OE Optical Engineering

RESEARCH PAPER

Experimental and computational investigation of Shack–Hartmann wavefront sensor measurements through a free shear layer

Jonathan Wells,[a,*] Matthew Kalensky,[b] R. Mark Rennie,[c] and Eric J. Jumper[c]

[a]Naval Information Warfare Center Atlantic, Quantum and Applied Optics, Hanahan, South Carolina, United States

[b]Naval Surface Warfare Center Dahlgren Division, Integrated Engagement Systems Department, Dahlgren, Virginia, United States

[c]University of Notre Dame, Institute of Flow Physics and Control, Notre Dame, Indiana, United States

ABSTRACT. Experimental Shack–Hartmann wavefront sensor (SHWFS) measurements were collected for a laser beam that propagated through a weakly compressible shear layer. Complementary computational fluid dynamics (CFD) was also conducted to match the experiment. The path-integrated CFD results were then applied to a SHWFS model such that the experimental and CFD results could be compared. Using both the experimental and CFD wavefront results, it was found that, although the CFD results slightly overestimated the resultant wavefront error, the CFD and experimental results revealed extremely similar wavefront topology. In order to further examine the aberrations imposed onto the laser beam in both datasets, the SHWFS image-plane irradiance patterns and circulation of phase gradients were studied. Similar to the overall wavefront topology, these data reduction approaches revealed similar phenomena in both the experimental and CFD-modeled results. Specifically, appreciable circulation and beam spread of the SHWFS image-plane irradiance patterns were exhibited throughout the shear layer's braid region. Both of these findings suggest that sharp phase gradients exist in the weakly compressible shear layer and both (1) the SHWFS resolution and (2) the continuous nature of the phase estimate obtained using SHWFS data in a least-squares reconstruction algorithm make these phase gradients challenging to resolve. The findings presented here inform efforts looking to experimentally or computationally study aero-optical environments.

Keywords: aero-optics; aero-effects; wavefront sensing; shear layers; wind-tunnel testing

Paper 20230882G received Sep. 18, 2023; revised Dec. 27, 2023; accepted Jan. 3, 2024; published Jan. 24, 2024.

1 Introduction

There has been growing interest in the development of aircraft-mounted laser propagation systems. To steer the laser beam used in such systems, beam directors that are hemispherical in shape have been heavily researched due to their fairly simple geometry and wide field of view. However, these hemispherical-turret beam director geometries are not aerodynamically benign. The protrusion of the turret into the freestream flow creates a complicated turbulence environment, which can degrade the performance of these optical systems.[1–10] The optical-turbulence

*Address all correspondence to Jonathan Wells, jonathan.d.wells2.civ@us.navy.mil

environment, which is caused by aerodynamic turbulence, is colloquially referred to as aero optics.[11–13]

Laser beam propagation through shear layers has been one aero-optical environment of particular interest. A shear layer forms from a shear or velocity gradient between two parallel streams of fluid. For the case of the turret, the separated low-pressure region aft of the turret forms a shear layer with the freestream flow.[2] The optical aberrations associated with this environment tend to have large amplitudes at inherently high temporal frequencies. When a laser beam is propagated from an optical turret at backward-looking angles, these so-called aero-optical aberrations imposed onto the laser beam (1) severely degrade the performance of laser propagation systems and (2) are challenging to compensate for using conventional approaches.

In order to better understand the underlying physics associated with these aero-optical aberrations, extensive lab-based[2–5,7,8,14–21] and aircraft-based[6,22–30] testing has been conducted in recent years. Although many foundational aero-optical experiments and analyses have been conducted, there is still much to learn about the coupling of fluidic properties and optical aberrations. Due to the high-speed nature of aero-optical environments, experimentation is often challenging and costly. Furthermore, the sensors that are employed to collect data have limitations. Recognizing the challenges associated with experimentation to explore the breadth of aero-optical experiments of interest, computational fluid dynamics (CFD) has been employed in recent years.[31,32]

In this paper, experiments and complementary CFD were conducted to explore the aero-optical aberrations associated with a free shear layer. Here, a shear layer was created in the Notre Dame Compressible Shear Layer Wind Tunnel (CSLWT). The CSLWT is an indraft transonic wind tunnel facility designed to produce a weakly compressible shear layer with a convective Mach number $M \approx 0.35$. A laser beam was propagated in the spanwise direction through the free shear layer and a Shack–Hartmann wavefront sensor (SHWFS) was used to measure the optical aberrations imposed onto the beam. The SHWFS is comprised of an array of subaperture lenslets situated in front of a measurement camera. The average gradient of the incoming phase aberration over each discrete lenslet is estimated from the resultant shifted irradiance patterns in the image plane. The deviations of these image-plane irradiance patterns away from their on-axis locations as well as the focal length of the lenslet subapertures allows the pupil-plane tilt of each subaperture to be estimated.[33,34] These measured tilt estimates can then be used in a least-squares reconstructor to estimate the continuous optical-path difference (OPD) aberration.

The simulations described in this paper were performed using ANSYS Fluent, and the simulation parameters were chosen to match experimental conditions in the Notre Dame CSLWT. Using the simulated two-dimensional flow field, the propagation of a laser beam through this shear-layer environment was modeled using basic principles. Afterwards, the resultant complex-optical field of the beam was applied to a SHWFS model.[24] Here, the pupil-plane complex-optical field was discretized into an array of subaperture lenslets. A thin-lens transmittance function was then applied to each subaperture and angular-spectrum propagation was used to obtain irradiance patterns in the image plane. As such, the simulated versus experimentally acquired SHWFS measurements could be directly compared.

In previous work where similar experiments were conducted,[35–37] observed differences between experimental and computational results were discussed. Specifically, it was shown that when experimental SHWFS measurements were used in a least-squares reconstructor, the resultant OPD estimate did not reveal the presence of sharp gradients in the braid region between the coherent vortical structures. Rather, the reconstructed OPD field showed smooth gradients. However, the simulated density fields did reveal steep, nearly discontinuous gradients at the slip line (the boundary between the high- and low-speed flows). In this paper, the authors further examine the similarities and differences between experimental and computational results. To do so, in addition to analyzing the experimental and computational OPD fields, (1) the second-moment statistics of the SHWFS' image-plane irradiance patterns are investigated,[34,38] and (2) the circulation of the measured slopes is calculated. These analyses were conducted on both the experimentally acquired SHWFS measurements as well as the SHWFS measurement simulated from the CFD output.

This paper is organized as follows: Sec. 2 introduces necessary background information regarding both the circulation of phase gradients and beam-spread approaches. Section 3.1

discusses the computational models used to simulate a weakly compressible shear layer. In Sec. 4, experimental facilities and the optical setup are discussed. Section 5 shows experimental and computational results, along with a discussion of the findings. Finally, Sec. 6 provides a conclusion for this paper.

2 Background

This section is intended to provide a brief introduction of underlying methodologies and concepts that are used in later sections to facilitate discussion of the results.

2.1 Optical Propagation Through a Shear Layer

In both experiment and simulation, a laser beam was propagated through a free shear layer in order to investigate the turbulence-induced phase aberrations imposed onto the beam. Here, the onset of Kelvin–Helmholtz instabilities leads to a transition to turbulent flow, which results in the pressure fluctuations along the slip line. Through the ideal gas law, these pressure fluctuations give rise to density fluctuations. Subsequently, density is related to the index of refraction through the Gladstone–Dale relation, given as

$$n'(x,y,z,t) = 1 - K_{\mathrm{GD}}(\lambda)\rho'(x,y,z,t), \tag{1}$$

where n' are the index-of-refraction fluctuations, ρ' are the density fluctuations, and $K_{\mathrm{GD}}(\lambda)$ is the Gladstone–Dale constant, which is a function of the laser wavelength λ.[12] For the purposes of the work presented here, a constant wavelength was used. As such, the wavelength dependence is dropped from K_{GD}, and we take $K_{\mathrm{GD}} = 2.27 \times 10^{-4}$ m^3/kg, which is valid for wavelengths in the visible to near infrared range.[39] The optical path length (OPL) is often used to quantify the severity of the aberrations imposed onto a laser. The OPL is defined as the path integral of the index of refraction:

$$\mathrm{OPL}(x,y,t) = \int_{z_1}^{z_2} n(x,y,z,t)\mathrm{d}z, \tag{2}$$

where $\hat{z}$ is the propagation path direction.[12,40] The OPD is the result of removing the spatial mean (or piston) from the OPL, given by

$$\mathrm{OPD}(x,y,t) = \mathrm{OPL}(x,y,t) - \overline{\mathrm{OPL}(x,y,t)}. \tag{3}$$

2.2 Shack–Hartmann Wavefront Sensor Data Reduction

As discussed in Sec. 1, the slopes measured from SHWFS image-plane irradiance pattern deflections are often used in a least-squares reconstructor to estimate the continuous OPD aberration across the pupil. However, it has been shown that higher-order aberrations (aberrations smaller than the size the SHWFS lenslet), nonuniform illumination, and phase discontinuities all degrade the OPD estimate.[34,38] For the purposes of the work presented here, it is not expected that nonuniform illumination or higher-order aberrations will appreciably affect the measurements. However, as discussed above, CFD has shown that sharp density gradients (and consequently sharp phase gradients) can present themselves along the slip line and braid region of a free shear layer. Since, by its nature, the reconstructed OPD field is blind to phase discontinuities, alternative means need to be employed to study the optical aberrations of the slip line and braid region. The sections to follow introduce two methods employed to do so; namely, the beam-spread approach and the circulation of phase gradients approach. It is important to note that these methods do not address the coupling effects between the least-squares reconstruction algorithm and SHWFS resolution, as that is beyond the scope of this work.

2.2.1 *Beam-spread approach*

It has recently been shown that when shock-wave-induced phase discontinuities[38,41] as well as branch-point-induced phase vortices[34,42,43] are located within the SHWFS subaperture lenslet pupils, there is appreciable beam spreading in the resultant image-plane irradiance patterns. Therefore, it is also expected that if sharp shear-layer-induced phase gradients intersected the

SHWFS subaperture pupils, and the SHWFS lenslet resolution is coarse, similar localized beam spreading would be observed. As such, by quantifying beam spread for each SHWFS irradiance pattern, thresholding can be employed to determine which irradiance patterns exhibit sufficient beam spread to indicate a sharp phase gradient was present across the lenslet pupil. The second-moment beam width, also referred to as $D4\sigma$, is one metric for quantifying beam spread.[44] The equation for $D4\sigma$ in the x dimension is given as

$$D4\sigma_x = 4\sqrt{\frac{\int_{-\infty}^{\infty}\int_{-\infty}^{\infty} I(x,y)(x-\bar{x})^2 \mathrm{d}x\,\mathrm{d}y}{\int_{-\infty}^{\infty}\int_{-\infty}^{\infty} I(x,y)\mathrm{d}x\,\mathrm{d}y}}, \tag{4}$$

where $I(x,y)$ is the image-plane irradiance pattern and $\bar{x}$ is the centroid location of the beam. A similar equation can be written for $D4\sigma_y$. It is often convenient to report an overall $D4\sigma$, which can be accomplished by $D4\sigma = \sqrt{D4\sigma_x^2 + D4\sigma_y^2}$. $D4\sigma$ was calculated for each image-plane irradiance pattern for both the experimental and computational SHWFS measurements. Here $D4\sigma$ was normalized by the diffraction-limited spot size for square apertures, $D_{\mathrm{DL}} = 2f\lambda/d$, where f is the focal length of the lenslets, λ is the wavelength of the beam, and d is the diameter of the SHWFS lenslet pupils.

2.2.2 *Circulation of phase gradients approach*

Fried and Vaughn[45] introduced an approach that calculated the circulation of phase gradients given as

$$\Gamma = \oint_C \nabla\phi \cdot \mathrm{d}r, \tag{5}$$

in order to identify branch points (turbulence-induced optical vortices). Here, phase gradients were summed along a closed-loop path and if the phase gradients summed to zero (in practice, $\sim$0), it was said that the local phase field was continuous. However, if summing the phase gradients along the closed-loop path resulted in a value significantly greater than zero, it was said that at least one phase singularity must exist within the contour. This approach has since been employed on SHWFS measurements to identify branch points.[43] However, instead of using the circulation of phase gradients to identify branch points from SHWFS measurements, this approach was used here to identify localized regions where the shear layer gives rise to optical vortices. For both the experimental and computational SHWFS measurements presented in this paper, Eq. (5) was applied to 2×2 adjacent subapertures using the x and y slopes calculated from irradiance pattern deflections with the lenslet focal lengths. The circulation value calculated at each 2×2 location was recorded.

3 Computational Models

This section will discuss the computational simulations performed in this paper, including model setup and parameters, and a discussion of methodology.

3.1 ANSYS Fluent

An unstructured computational grid was created and run in ANSYS Fluent to simulate the CSLWT conditions. A schematic showing computational parameters is shown in Fig. 1.

Here the subscript 1 refers to the high-speed flow region, and the subscript 2 refers to the low-speed flow region. The parameter P represents pressure, and T represents temperature; the subscript s represents the static quantity while the subscript T represents the total quantity.

The computational domain extends ± 1.5 m vertically from the centerline and has a length of 5 m to allow adequate room for shear layer growth. This helps to ensure that the shear layer development is not influenced by the boundary conditions of the computational domain. The minimum grid size, which was located at the origin of the shear layer, was on the order of 0.5 mm and was selected in accordance with the discussion provided in Ref. 31. Specifically, the smallest shear layer eddies were estimated from the convection length Δ_n corresponding to the initial shear layer natural frequency f_n as

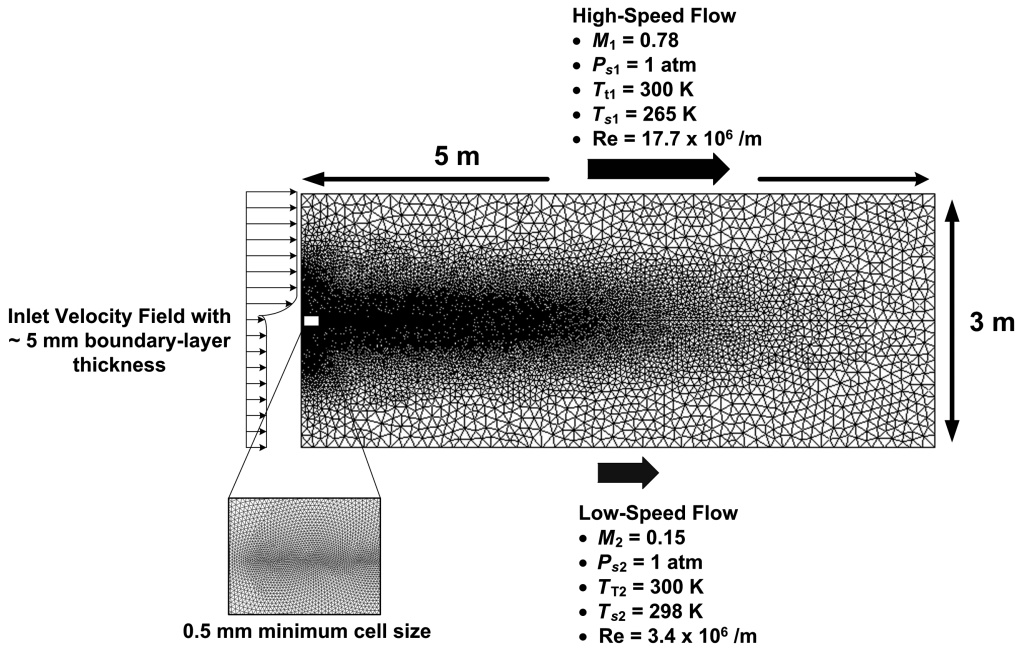

Fig. 1 Example of fluent grid and boundary conditions. The high-speed flow (top) is ≈259 m/s, and the low-speed flow (bottom) is ≈52 m/s.

$$\Delta_n = \frac{U_{cn}}{f_n}, \tag{6}$$

where U_{cn} is the shear layer convective velocity:

$$U_{cn} = \frac{(U_1 + U_2)}{2}, \tag{7}$$

where U_1 and U_2 represent the high-speed and low-speed velocities, respectively.

In Eq. (6), f_n depends on the momentum thickness of the boundary layer feeding the high-speed side of the shear layer[46] and is described by linear stability theory as

$$\frac{2f_n\Theta}{U_1} = 0.036. \tag{8}$$

The boundary layer parameters chosen for the high-speed flow were a boundary layer thickness of $\delta = 5$ mm and a momentum thickness of $\Theta \approx 5$ mm. These values were selected as they matched experimental measurements of the splitter plate boundary layer made in the CSLWT.[31,47,48] Combining Eqs. (6) and (8), these boundary layer parameters give $f_n \approx 10$ kHz and $\Delta \approx 14$ mm for the smallest eddies. Hence, the 0.5 mm grid size prescribed in the computational model from Fig. 1 gives $\tilde{3}0$ grid points for the smallest eddies.

Constant static pressure conditions were used at the upper and lower boundaries of the computational domain to establish free-stream conditions outside the field of interest. These conditions were also enforced at the inlets (high and low speed), and a velocity profile was applied at the incoming centerline to simulate a boundary layer on the shear layer splitter plate.

Viscous heating was enabled as Fluent's default form of the energy equation in pressure-based solvers does not include the viscous dissipation terms (viscous heating is often negligible). In most flows, viscous heating only becomes important when the Brinkman number, Br, given as

$$\mathrm{Br} = \frac{\mu U_e^2}{k\delta T} \tag{9}$$

approaches or exceeds unity. Here, μ is the dynamic viscosity, U_e is the flow velocity, k is the thermal conductivity, and T is the static temperature. Compressible flows typically have $\mathrm{Br} \geq 1$ and although the flow of interest in this work has been defined as weakly compressible, prior analysis[31] showed that viscous work is negligible in the braid regions. Therefore, the addition of

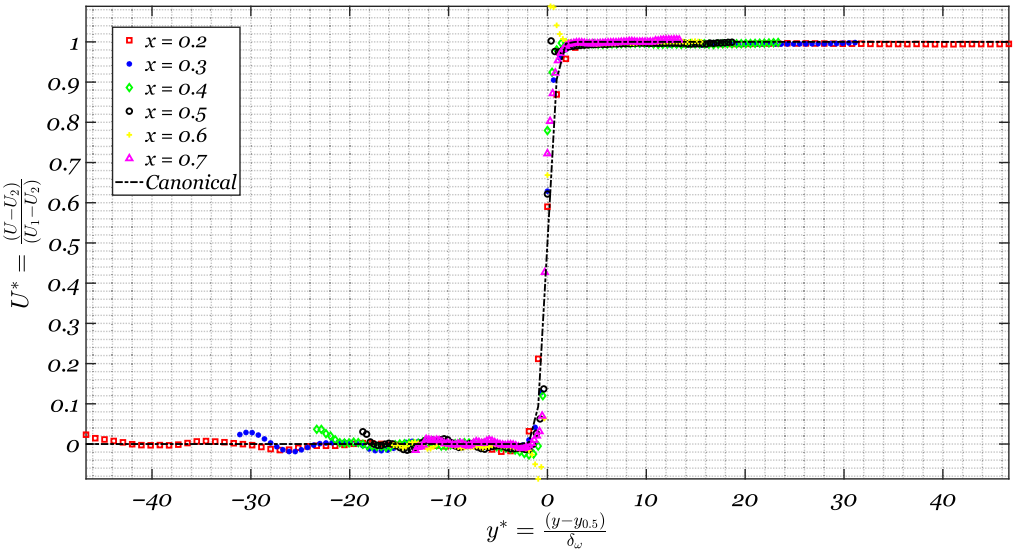

Fig. 2 Nondimensional shear layer velocity profiles.

this option should have no effect on the thermodynamic solution for the shear layer flow; rather, this term is expected to only have a small influence on the energy equation in the vicinity of the vortex cores.

The simulation was run for a total time of 4 s, with a time step, $dt = 1 \times 10^{-6}$ s. The nondimensional velocity profiles are provided in Fig. 2. Here the x axis is the vertical coordinate (referenced to the shear layer slip line location) normalized by the shear-layer vorticity thickness $y^* = \frac{y-y_{0.5}}{\delta_w}$, where $y_{0.5}$ is vertical coordinate of the shear layer slip line, and δ_ω is the shear layer vorticity thickness described by

$$\delta_\omega = \frac{U_1 - U_2}{\left(\frac{dU}{dy}\right)_{\max}}. \tag{10}$$

The y axis of Fig. 2 is the normalized velocity profile $U^* = \frac{U-U_2}{U_1-U_2}$.

The velocity profiles from the Fluent solution collapse and agree with the canonical shear layer profile given in Ref. 31. Using the velocity profiles from the Fluent shear layer results presented in Fig. 2, the shear layer vorticity was computed using Eq. (10). The growth of δ_ω as a function of streamwise location x is plotted in Fig. 3.

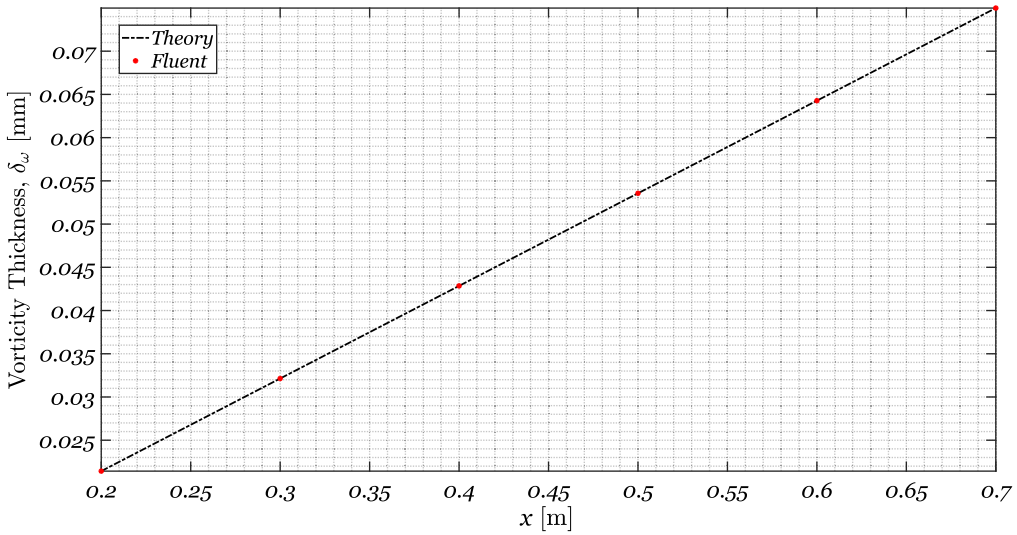

Fig. 3 Shear layer vorticity thickness development.

Figure 3 shows that the shear layer vorticity thickness from the Fluent solution grows linearly with streamwise location and is in agreement the fit given by

$$\frac{\delta_\omega}{x} = 0.17\frac{1-r}{1+r}, \tag{11}$$

where $r = U_2/U_1$ is the velocity ratio across the shear layer.

3.2 Two-Dimensional Versus Three-Dimensional Simulations

It is important to note that these simulations were performed as two-dimensional simulations and thus capture only the effects of large-scale turbulence. Specifically, as described in Ref. 49, two-dimensional shear layer simulations accurately capture the large-scale vortex behavior in the shear layer but do not capture smaller-scale turbulent structures. Although small-scale turbulence does contribute to the system total energy, as well as the localized behavior of particle inertia, it does not affect the primary mechanism of vortex growth in free shear layers or the large-scale thermodynamic behavior in regions without large-scale structures, such as the braid regions. Three-dimensional DES simulations of a weakly compressible shear layer can be found in the literature,[50] which show that, even with the presence of small-scale turbulence, large-scale vortical structures are not affected until much further downstream, and the thermodynamic discontinuities discussed in this work and in the previous work[31] are still present.

4 Experimental Setup

This section will discuss the facilities used to collect experimental data in this paper, including wind tunnel configuration and optical setup.

4.1 Wind Tunnel Facility

All experimental data were obtained in Notre Dame's WCSLT. The facility is comprised of an indraft transonic tunnel and a test section made up of a high-speed and a low-speed inlet. The high-speed inlet produces a freestream Mach number of $M \approx 0.75$, and the low-speed inlet produces a freestream Mach number of $M \approx 0.35$. With typical laboratory conditions, these flow speed Mach numbers equate to a high-speed flow of $U_1 \approx 259$ m/s and a low-speed flow of $U_2 \approx 52$ m/s. A key feature of the wind tunnel is that flow into the low-speed side of the wind tunnel passes through a "straw box" section of closely spaced tubes, which reduces the total pressure of the flow in the low-speed side such that the static pressure is uniform in the test section. Furthermore, both the high- and low-speed inlets draw air from the same laboratory environment ensuring that total temperature is also matched. This configuration creates a weakly compressible shear layer with a convective Mach number of $M_c \approx 0.35$ calculated using the convective velocity from Eq. (7).

The test section is 0.0762 m (3 in.) in width, with a splitter plate mounted at the intersection of the high- and low-speed inlets. Three voice-coil actuators are located in the splitter plate, which are driven by an amplified signal from a function generator. These voice-coil actuators serve to "force" the shear layer at a defined frequency, which regularizes the shear layer's coherent structure frequency at a specific location downstream of the splitter plate.[47]

The boundary layer in the high-speed flow at the edge of the splitter plate was measured to be ~10 mm. The turbulent boundary layer thickness for the sides of the wind tunnel test section was then estimated using

$$\frac{\delta}{x} \approx \frac{0.38}{(\mathrm{Re}_x)^{\frac{1}{5}}}, \tag{12}$$

where Re_x is the Reynolds number.[51] Using this approach, the turbulent boundary layer thickness at the streamwise measurement location in the test section was estimated to be 21 mm. This value was then used in the computational simulations to more accurately compute path-integrated OPD values from the simulated density field.

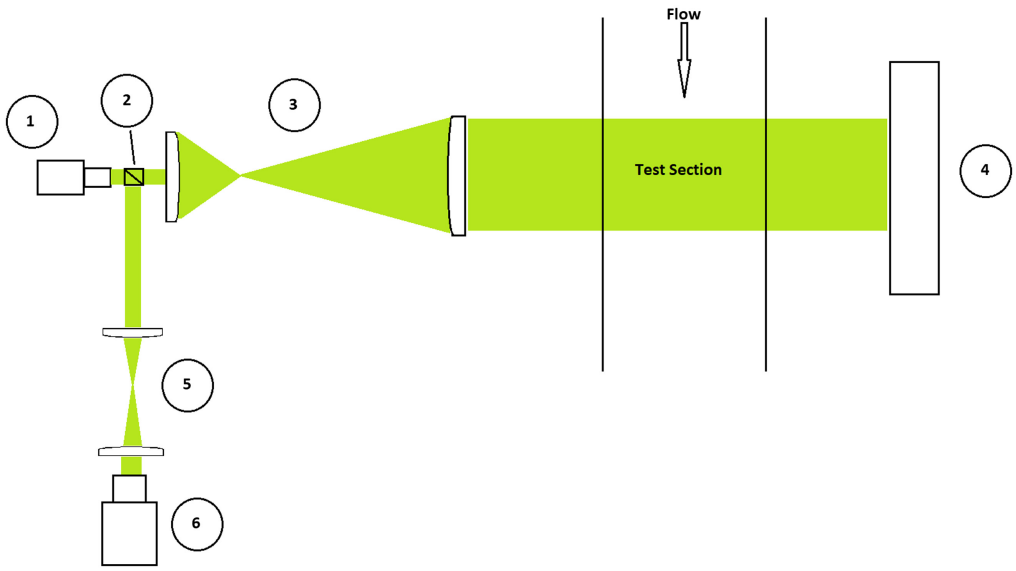

Fig. 4 Diagram of the wavefront optics setup used to obtain experimental results in this dissertation. (1) 25.4 mm (1 in.) collimator, (2) 50/50 beam splitter cube, (3) 254 mm (10 in.) beam expander, (4) large return mirror, (5) reimaging telescope, and (6) high-speed camera with SHWS.

4.2 Optical Setup

In these experiments, a beam was propagated in the spanwise direction through the shear layer created in the WCSLT. SHWFS measurements were collected, and streamwise OPD was reconstructed using a least-squares reconstruction method.[52] The optical configuration for the SHWFS measurements is shown in Fig. 4.

Here a 532 nm continuous wave laser was collimated to 25 mm (1 in.), then passed through a 254 mm (10 in.) beam expander. The expanded beam was passed through the WCSLT optics window and was reflected off a 305 mm (12 in.) return mirror mounted on the other side. The reflected beam was then sent back through the same optical path (a double-pass configuration), split at the beam splitter, and sent through a relay telescope, which reimaged the wavefront at the return mirror onto the wavefront sensor.

SHWFS irradiance patterns were recorded using a Vision Research v1611 high-speed camera at 49 kHz and 512×512 resolution. The camera exposure time was set to 0.38 μs to minimize the effects of frame blurring due to the relatively high flow velocities. The microlens array used for data collection consisted of $\sim 80 \times 67$ lenslets with a 300 μm pitch and focal lengths of $f = 40$ mm.

5 Results and Discussion

This section presents experimental SHWFS results, alongside an evaluation of beam spread and phase gradient circulation within the experimental results. The computational results are presented next, which show the primitive fields computed from the CFD simulations discussed in Sec. 3.1 and the results of simulated SHWFS measurements of the ANSYS Fluent density field. Similar to the experimental results, beam spread and phase gradient circulation are examined. Finally, a comparison between the experimental and computational results is given.

5.1 Experimental Results

Data reduction was accomplished using in-house processing codes. Specifically, the SHWFS images were used to calculate centroid locations of the image-plane irradiance patterns that yielded x and y slopes. Beam spread of the individual SHWFS image-plane irradiance patterns was also calculated using Eq. (4) and the circulation of phase gradients was calculated from the x and y slopes using Eq. (5). The slopes were also used to estimate the continuous OPD field using a least-squares reconstructor, in this case using the Southwell geometry.[52] The resultant reconstructed OPD fields were postprocessed both with and without tip, tilt, and piston. An additional

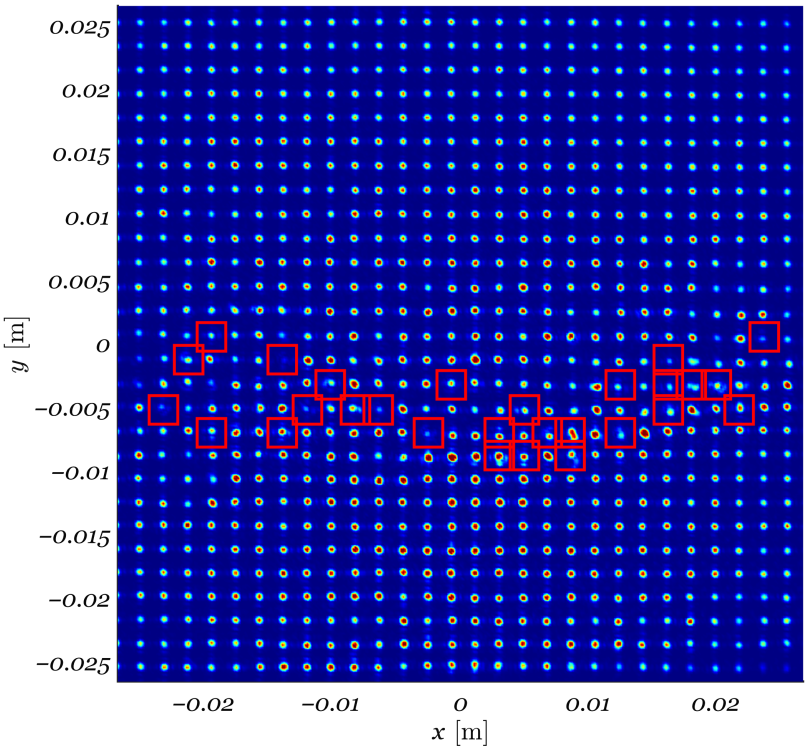

Fig. 5 Single frame of experimentally obtained SHWFS image-plane irradiance patterns. Red squares indicate irradiance patterns where appreciable beam spreading was measured. Flow is from left to right, with the high-speed flow at top and low-speed flow at the bottom.

postprocessing step was taken, in which the time-averaged mean of the tip/tilt-removed data was subtracted from the tip/tilt-retained data to obtain a mean-removed but cross-stream (vertical) tip restored result. This additional postprocessing step was performed in order to retain the larger OPD value for the portion of the beam passing through the less dense, low-speed flow (and vice versa for the high-speed flow). This allowed for comparison of the data to the OPD fields associated with the density fields, and the gradient in the density fields, for the computational simulations.

Figure 5 shows the SHWFS image-plane irradiance patterns from a single frame of the measurement data. Using the beam-spread approach discussed in Sec. 2.2.1, $D4\sigma/D_{DL}$ was calculated for every SHWFS image-plane irradiance pattern. A beam-spread threshold of $D4\sigma/D_{DL} = 1.7$ was imposed for the experimental measurements. As such, irradiance patterns where the calculated $D4\sigma/D_{DL}$ exceeded the beam-spread threshold were flagged by the algorithm. The flagged image-plane irradiance patterns are depicted in Fig. 5 using red squares.

Figure 5 shows that multiple pupil locations reveal appreciable spreading of the resultant image-plane irradiance patterns throughout the flow field. In particular, the beam spreading behavior is present along a sinusoidally shaped line through the center of the figure, indicating sharp gradients in regions consistent with the shear layer slip line location.

The x and y slopes calculated from the SHWFS image-plane irradiance patterns were then used in a least-squares reconstruction algorithm in order to estimate the continuous OPD field. Figure 6 shows the resultant reconstructed OPD field associated with the SHWFS measurement displayed in Fig. 5. The OPD field is displayed in units of meters.

A prominent vortex core can be seen in the center of Fig. 6, which can be related to the circular pattern of red boxes from $0 < x < 0.01$ on the x axis of Fig. 5. It is important to note that there are no sharp changes in the OPD field surrounding the vortex core in Fig. 6. In fact, the entire reconstructed OPD field reveals smooth gradients, even in the spatial locations along the braid region of the shear layer. Using the reconstructed OPD field, the $\mathrm{OPD}_{\mathrm{RMS}}$ was computed by taking the root-mean-square over the spatial dimensions and then averaging through time. After

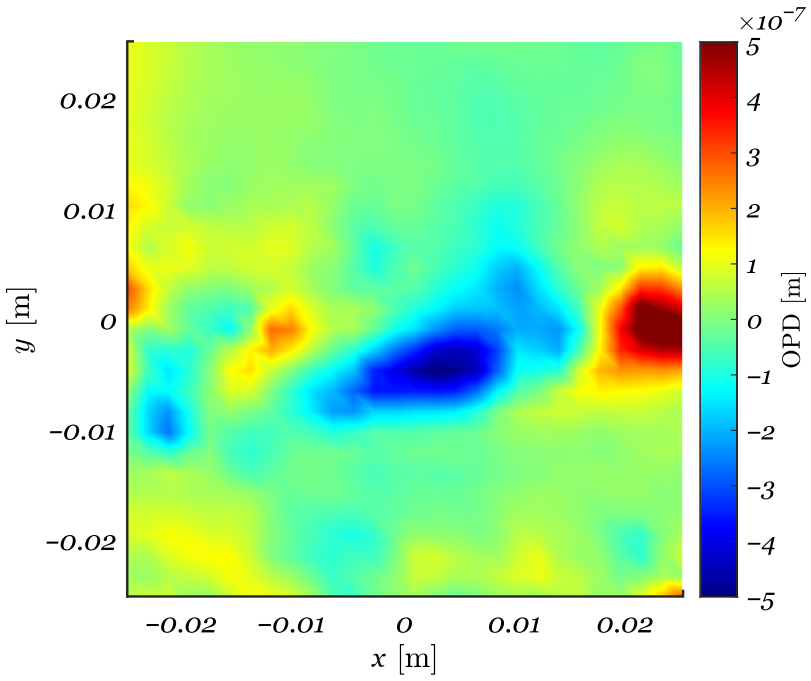

Fig. 6 Experimental SHWFS OPD reconstructed using a least-squares algorithm. Flow is from left to right, with the high-speed flow at top and low-speed flow at the bottom.

doing so, the calculated reconstructed $\mathrm{OPD}_{\mathrm{RMS}}$ was found to be 1.40×10^{-7} m, which was in agreement with scaling proposed in Ref. 53.

To further investigate the optical aberrations along the slip line of the shear layer, an examination was performed of the beam spread and circulation of phase gradients associated with the SHWFS measurement presented in Fig. 5. These results are presented in Fig. 7. Figure 7(a) shows the calculated $D4\sigma/D_{\mathrm{DL}}$ values, and Fig. 7(b) shows where the beam-spread algorithm flagged SHWFS irradiance patterns, which exceeded the beam-spread threshold.

Appreciable image-plane irradiance pattern beam spreading was measured along the entire slip line. As discussed in Sec. 2.2.1, if it is assumed the SHWFS pupil is uniformly illuminated and higher-order aberrations are negligible, then beam spread associated with the SHWFS image-plane irradiance patterns is likely associated with sharp phase gradients or discontinuities within the SHWFS lenslet pupils; this suggests the presence of these sharp phase gradients in the measurements presented in Fig. 5. Furthermore, as discussed in Ref. 38, when a pupil-plane discontinuity causes appreciable beam spreading or bifurcation of the resultant image-plane irradiance pattern, the slopes estimated from the x and y deflections of the irradiance pattern become poor estimates of the local phase tilt across the pupil. Specifically, the slopes measured from the SHWFS image-plane irradiance patterns underpredict the local slopes in areas where appreciable beam spreading is evident. Subsequently, the reconstructed OPD field underpredicts changes in OPD within the pupil. This result is particularly noticeable in the left portion of the reconstructed OPD field presented in Fig. 6. Here, the shear-layer-induced aberrations are fairly low amplitude with small-scale spatial structure. However, since significant beam spreading was measured here, the reconstructed OPD in this region was likely strongly attenuated and corrupted. Therefore, the small-scale structures observed in the reconstructed OPD field are nonphysical. In fact, closer examination of Fig. 5 suggests a large circulation region in the left portion of the flow field, which is not captured by the least-squares reconstruction algorithm. Such a result can be attributed to the combination of two factors: first, that beam spread over a significant spatial area may corrupt reconstructed OPD fields such that coherent fields are not accurately visualized. Second, the spatial resolution of the measurement itself is insufficient to resolve the smallest flow features on this scale. However, it should be noted that such structures were resolved in other regions of the flow field, thus contribution of error from such a spatial resolution is likely not the dominating factor in this case.

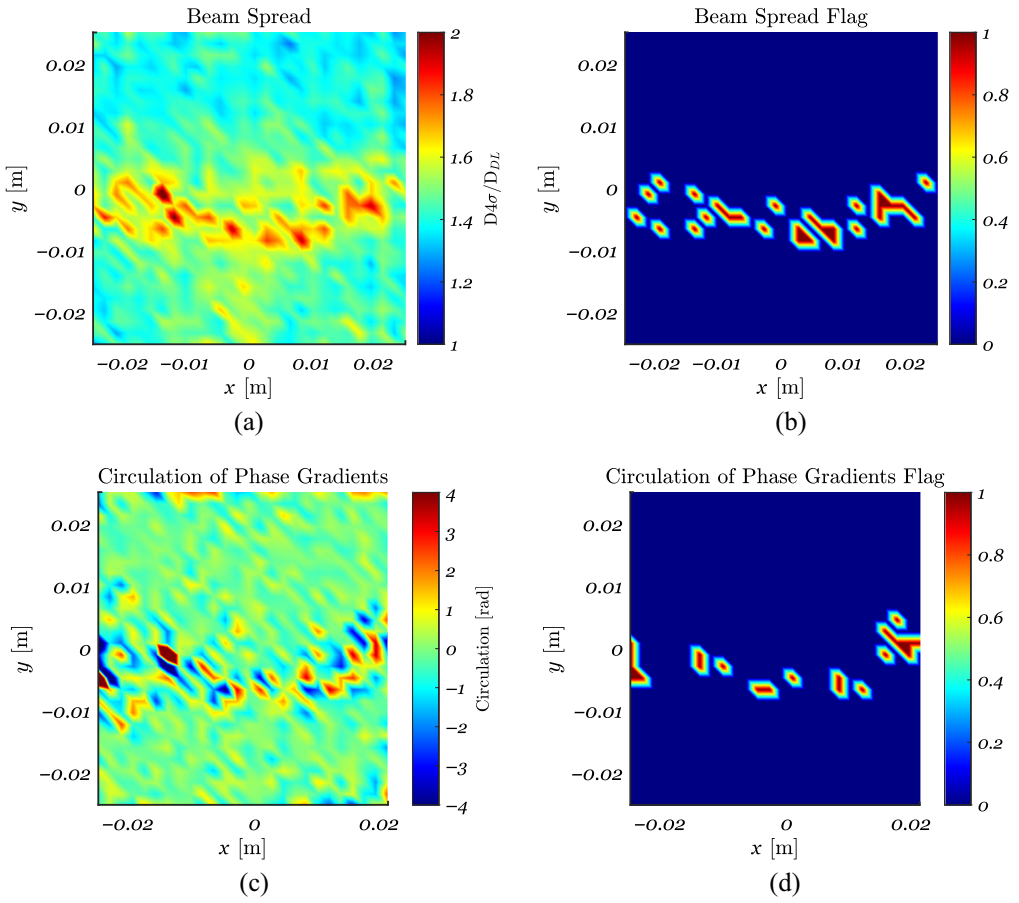

Fig. 7 (a, b) Image-plane irradiance pattern spreading and (c, d) results of phase curl analysis. In each image, flow is from left to right, with the high-speed flow at top and low-speed flow at the bottom.

To further explore the optical aberrations along the slip line of the shear layer, the circulation of phase gradients approach discussed in Sec. 2.2.2 was employed. The calculated circulation field is presented in Fig. 7(c) plotted in units of radians. Similar to the beam-spread flag presented in Fig. 7(b), a circulation threshold was imposed to determine locations where appreciable circulation was identified. For the experimental measurements, a circulation threshold of $|3|$ rad was imposed. Locations where the calculated circulation exceeded this threshold are plotted in the bottom-right plot of Fig. 7. These results show that most of the slip line exhibited appreciable circulation. Recall that locations where the calculated circulation is significantly >0 (approaching 2π rad) suggests the presence of optical vorticity within the contour used to calculate circulation.

5.2 Computational Results

In this section, the results of the computational simulations discussed in Sec. 3.1 are discussed. These results are presented in Fig. 8.

Here (a) represents the velocity field, (b) represents the density field, (c) represents the static-pressure field, (d) represents the total-pressure field, (e) represents the static temperature field, and (f) represents the total-temperature field. As discussed in Sec. 3.1, the static pressure and total temperature are matched on either side of the slip line. Additionally, the density field reveals sharp gradients in the braid region between coherent vortex structures.

5.3 Simulated Shack–Hartmann Wavefront Measurement Results

In this section, a portion of the simulated two-dimensional density field presented in the top-right plot of Fig. 8 was used to calculate an OPD field from which a simulated SHWFS model was applied. In order to do so, first, the index-of-refraction field was calculated from the density field using Eq. (1). Next, the index-of-refraction field was used to compute the OPL field using

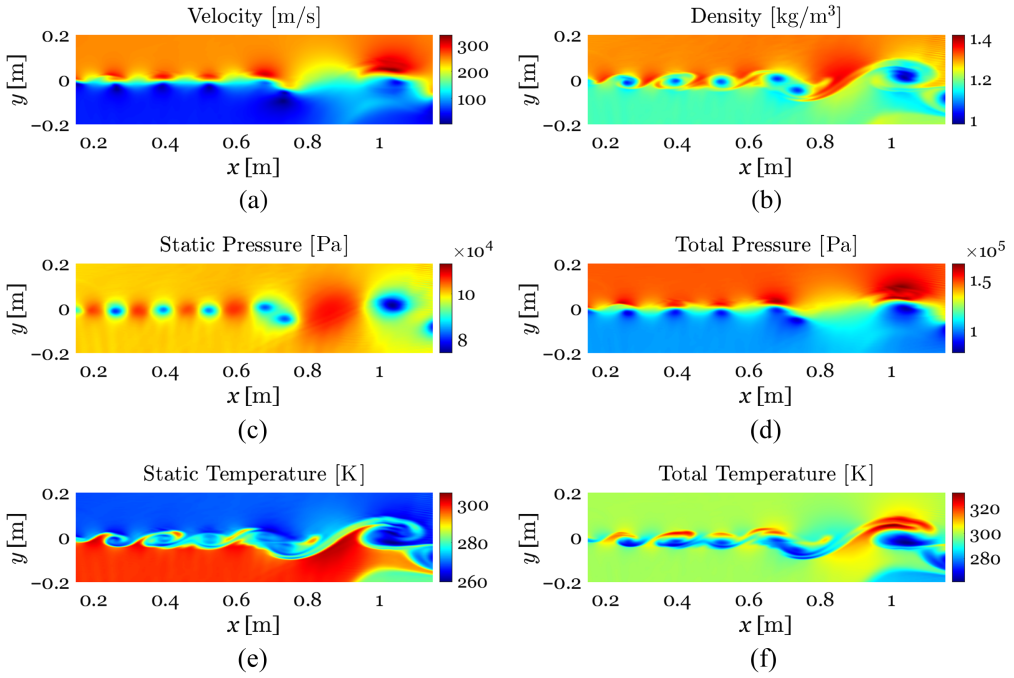

Fig. 8 (a) Velocity, (b) density, and static and total fields for (c), (d) pressure and (e), (f) temperature from fluent simulation. In each image, flow is from left to right, with the high-speed flow at top and low-speed flow at the bottom.

Eq. (2). In Eq. (2), the propagation distance Z was taken to be the width of the wind tunnel in the spanwise direction minus twice the boundary layer thickness of the wind-tunnel walls (discussed in Sec. 4.1) at the streamwise measurement location. In doing so, the net propagation distance used in Eq. (2) was 0.035 m where the wind-tunnel width was 0.076 m, and the boundary-layer thickness was estimated to be 0.021 m. The OPL field was then used to calculate the OPD field using Eq. (3). The resultant OPD field is presented in Fig. 9(a) in units of meters.

The OPD field contains sharp, nearly discontinuous gradients at the slip line in the braid regions, as expected, and is similar to the simulated density field. This OPD field was then used to compute an associated phase field as, $\phi = -2\pi \mathrm{OPD}/\lambda$. The calculated phase field is presented in the right plot of Fig. 9 in units of radians. Here, phase wraps are shown along the entire slip line confirming the presence of steep phase gradients.

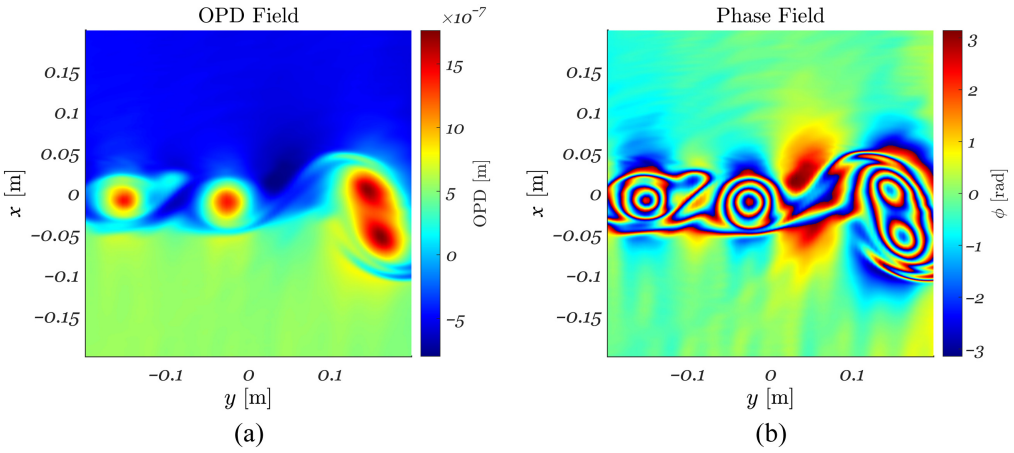

Fig. 9 (a) OPD field computed from CFD simulations. (b) Resultant phase field after propagating through the simulated flow field. In each image, flow is from left to right, with the high-speed flow at top and low-speed flow at the bottom.

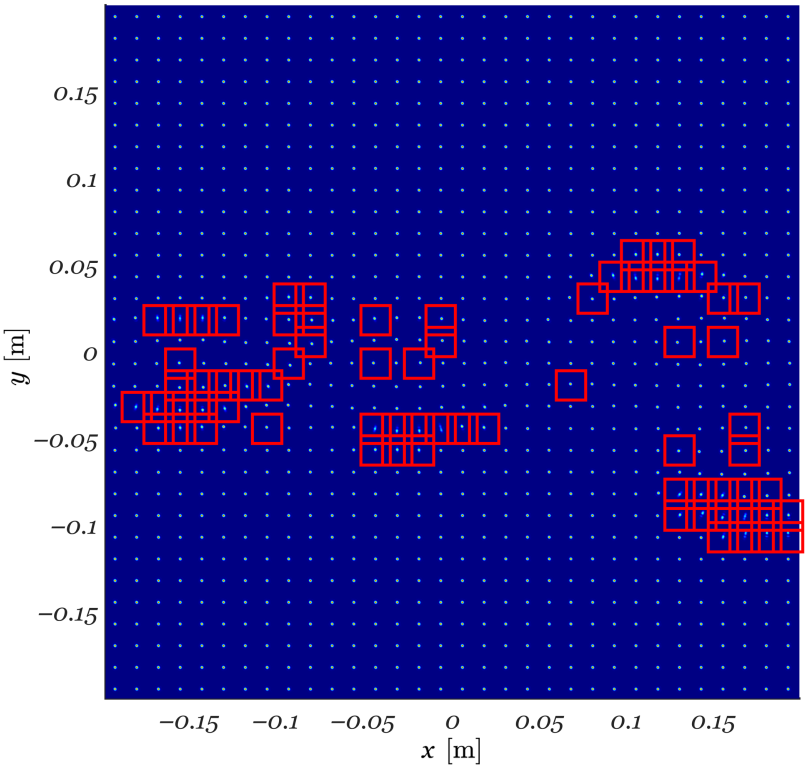

Fig. 10 SHWFS image-plane irradiance pattern for the simulated shear layer. Flow is from left to right, with the high-speed flow at top and low-speed flow at the bottom.

Uniform illumination was assumed across the simulated field presented in Fig. 9, and the computed phase field was used to simulate a complex-optical field and then applied to a SHWFS model. Here the pupil-plane complex-optical field was discretized into an array of square subaperture lenslets. A thin-lens transmittance function was then applied to each subaperture, and angular-spectrum propagation was used to obtain irradiance patterns in the image plane. The resultant simulated SHWFS image is presented in Fig. 10. Similar to the experimental results in Sec. 5.1, $D4\sigma/D_{\mathrm{DL}}$ was calculated for every SHWFS image-plane irradiance pattern and a beam-spread threshold of $D4\sigma/D_{\mathrm{DL}} = 2.9$ was imposed. The flagged image-plane irradiance patterns are depicted in Fig. 10 using red squares.

There is a visible trace of broken and highly spread image-plane irradiance patterns that follow the slip line between the high- and low-speed flows. In fact, it is possible to discern the vortex boundaries and braid regions by following the trace of stretched and broken irradiance patterns. This sharp line of distortions follows the sharp density discontinuity between the high- and low-speed flows that is predicted by Fluent. Using the simulated SHWFS image presented in Fig. 10, x and y slopes were calculated from the image-plane irradiance patterns and used in a least-squares reconstruction algorithm. The resulting reconstructed OPD field is presented in Fig. 11 in units of meters.

Although the OPD field presented in Fig. 9 revealed sharp phase gradients along the slip line, the least-squares reconstructed OPD field yielded a very different result. Namely, Fig. 11 shows that the resultant reconstructed OPD field shows no such gradients. In fact, the simulated reconstructed OPD field is nearly identical to the experimental SHWFS result presented in Fig. 6. This observation further implies that the least-squares reconstruction algorithm is poorly resolving sharp density gradients in flow fields of interest. Similar to the experimental results, the reconstructed OPD field was also used to compute $\mathrm{OPD}_{\mathrm{RMS}}$. The $\mathrm{OPD}_{\mathrm{RMS}}$ calculated from the simulated data was found to be 3.49×10^{-7} m. Although the $\mathrm{OPD}_{\mathrm{RMS}}$ calculated from the simulation results is slightly larger than the $\mathrm{OPD}_{\mathrm{RMS}}$ measured from experiment, this discrepancy continues to be investigated.

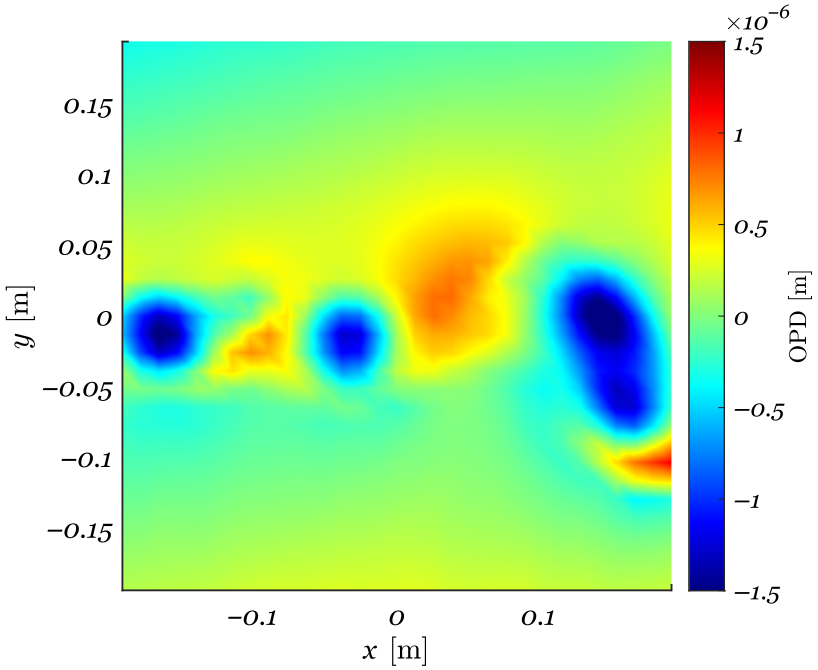

Fig. 11 Result of least-squares reconstruction of SHWFS measurement of a simulated shear layer. Flow is from left to right, with the high-speed flow at top and low-speed flow at the bottom.

Similar to the experimental results, the beam-spread and circulation of phase gradients approaches were also employed on the simulated SHWFS image. These results are presented in Fig. 12, where (a) presents the calculated beam-spread values, (b) presents the flagged locations due to exceeding the beam-spread threshold, (c) presents the circulation of phase gradient values, and (d) presents the flagged locations due to exceeding the circulation threshold. Here a circulation threshold of $|4|$ was used.

Given that the simulated SHWFS result (Fig. 11) is nearly identical to the experimental SHWFS results (Fig. 6), it was expected that this analysis would result in similar findings. Generally speaking, the beam spread and circulation of phase gradients results are similar to the experimental results but there are subtle differences worth noting. First, in the top-left plot of Fig. 12, the image-plane spreading was most prominent in regions in close proximity to vortex cores. The best example of this is the top and bottom of the vortex core on the far right portion of the frame; the sharp gradient that is rotating outside the vortex core shows significantly more beam spread than the vortex core itself. Second, the braid region between the middle and right vortices is much more pronounced in the circulation of phase gradients analysis, shown in the bottom-right plot of Fig. 12. When compared to the experimental results in Fig. 7, which show only minor phase discrepancy in the braid regions, the computational results in Fig. 12 show this pattern through the entire flow field. This result implies that there may be subtle differences between the computational and experimental flow fields, but there has been no work performed thus far to explore this discrepancy.

It is also worth noting that effects of spanwise nonuniformity of the shear layer within the wind tunnel test section were considered. In the event that the shear layer produced in the experimental test section was not reasonably spanwise uniform, the path-integrated results of the SHWFS measurements could potentially miss the sharp gradients due to the spatial-averaging nature of the measurement. However, it was shown that the test section used for the data collection in this paper produces shear layers with a relatively high spanwise correlation when forced.[53] Additional work[36] showed that spanwise nonuniformity up to ∼14% of the mean cross-stream variation had a negligible effect on the OPD field.

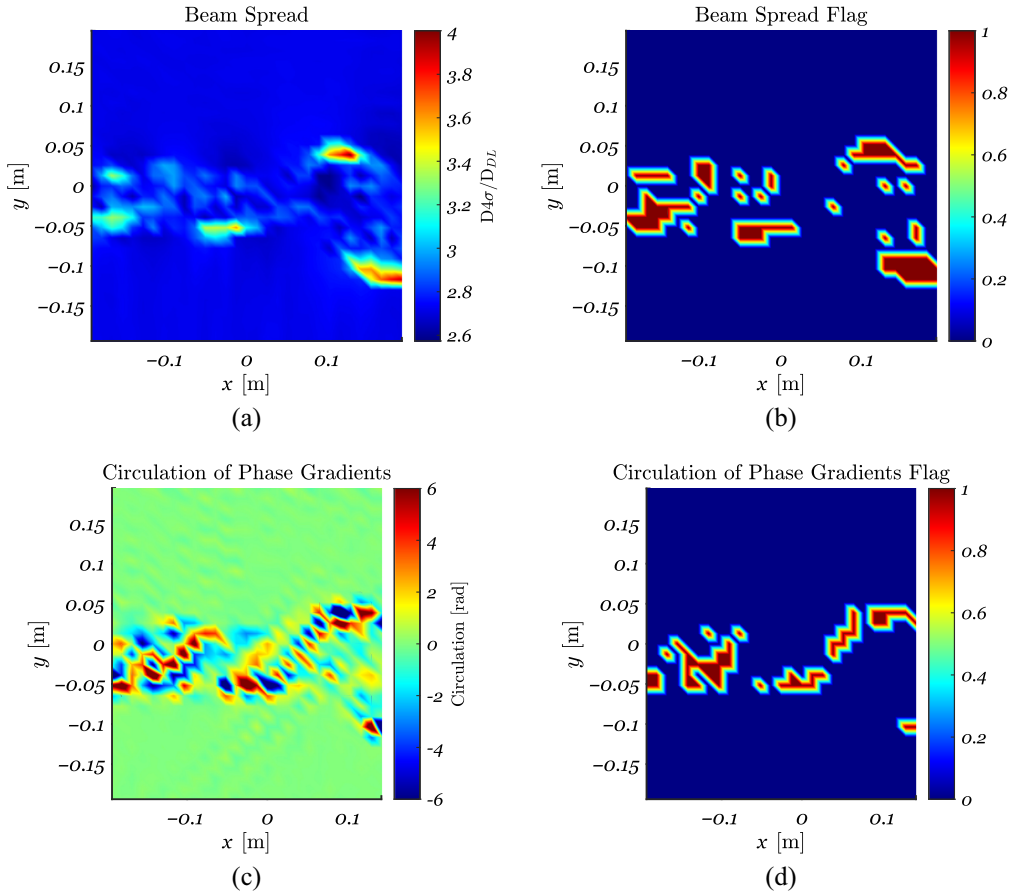

Fig. 12 (a) Beam spread analysis of the image-plane irradiance pattern. (b) Regions of the image-plane irradiance pattern that exceed a prescribed threshold for spatial spreading. (c) Circulation of phase gradients for the flow field of interest. (d) Regions of the flow field where the calculated circulation of phase gradients exceeded the threshold discussed in Sec. 2.2.2. In each image, flow is from left to right, with the high-speed flow at top and low-speed flow at the bottom.

6 Conclusions

An analysis of experimental wavefront data was shown, which displays stretching and splitting of image-plane irradiance patterns in SHWFS measurements of a weakly compressible shear layer. Experimental SHWFS measurements were shown to produce least-squares-reconstructed OPD fields that did not reveal sharp gradients in regions where sharp gradients were predicted by image-plane irradiance pattern beam spreading. Further analysis also suggested that the combination of the least-squares reconstruction algorithm and low spatial resolution proved incapable of resolving large-scale coherent structures in regions where several adjacent lenslets displayed significant beam spreading.

Computational results supported the experimental findings. Specifically, a simulated shear layer produced a density field with near-discontinuous gradients at the slip line between the high- and low-speed flows, and the resultant least-squares-reconstructed SHWFS OPD field was unable to resolve such gradients. In contrast, the directly computed OPD field [using Eqs. (1)–(3)] revealed sharp gradients. Furthermore, the phase field computed from this OPD field revealed many phase wraps along the entire slip line, consistent with the presence of sharp gradients.

An analysis of image-plane beam spread and circulation of phase gradients was conducted on both the experimental and computational SHWFS imagery, which showed similar results. Specifically, significant beam spreading was present in each instance at nearly every location along the shear layer slip line, consistent with sharp gradients in those locations.

The findings from the experimental and computational data presented in this paper suggest that sharp gradients within the braid region of a weakly compressible shear layer are not adequately resolved using low spatial resolution SHWFS data in a least-squares-based reconstruction algorithm. Although data presented in this paper imply that current least-squares methods are insufficient in their handling of such gradients, the SHWFS image-plane irradiance patterns contain much of the information that could be used to more completely characterize the optical-turbulence environment through which the beam propagated. Specifically, the image-plane irradiance pattern stretching and breaking provides information on gradient strength and direction, and the circulation of phase gradients analysis provides the locations within the flow where optical-phase vortices occur. Additionally, the data suggest that decreasing the area of interrogation within the flow field to achieve higher spatial resolution is necessary to determine the contribution of spatial resolution to the sharp gradient resolution capability. These results may inform future efforts looking to develop phase-discontinuity-tolerant reconstruction algorithms as well as efforts looking to continue to study the physics associated with laser beam propagation through a free shear layer.

Disclosures

The authors declare no conflicts of interest.

Code and Data Availability

Data underlying the results presented in this paper are not publicly available at this time but may be obtained from the authors upon reasonable request.

Acknowledgments

The authors would like to thank Dr. Matthew R. Kemnetz for many insightful discussions regarding the results presented within. This work was approved for public release; distribution is unlimited. Naval Information Warfare Center Atlantic public affairs release (Approval No. 2024-136).

References

1. S. Gordeyev et al., "Aero-optical environment around a conformal-window turret," *AIAA J.* **45**(7), 1514–1524 (2007).
2. S. Gordeyev and E. Jumper, "Fluid dynamics and aero-optics of turrets," *Prog. Aerosp. Sci.* **46**, 388–400 (2010).
3. N. De Lucca, S. Gordeyev, and E. Jumper, "The study of aero-optical and mechanical jitter for flat window turrets," in *50th AIAA Aerosp. Sci.*, American Institute of Aeronautics and Astronautics (2012).
4. S. Gordeyev et al., "Experimental studies of aero-optical properties of subsonic turbulent boundary layers," *J. Fluid Mech.* **740**, 214–253 (2014).
5. N. G. De Lucca et al., "Investigation of flow dynamics over turrets with different spanwise aspect ratios using PSP," in *SciTech Forum*, American Institute of Aeronautics and Astronautics (2018).
6. N. De Lucca, S. Gordeyev, and E. Jumper, "In-flight aero-optics of turrets," *Opt. Eng.* **52**, 071405 (2013).
7. M. Kalensky et al., "Investigation of aero-mechanical jitter on a hemispherical turret," *Proc. SPIE* **11836**, 1183606 (2021).
8. M. Kalensky et al., "Pressure sensitive paint measurements on a hemispherical turret," *Proc. SPIE* **11836**, 1183607 (2021).
9. T. J. Bukowski et al., "Modal analysis of pressure fields on and around turrets with different protrusions," *Proc. SPIE* **12239**, 122390F (2022).
10. A. L. Roeder and S. Gordeyev, "Wake response downstream of a spanwise-oscillating hemispherical turret," *J. Fluids Struct.* **109**, 103470 (2022).
11. K. Gilbert, *Aero-Optical Phenomena*, American Institute of Aeronautics and Astronautics, New York (1982).
12. E. J. Jumper and E. J. Fitzgerald, "Recent advances in aero-optics," *Prog. Aerosp. Sci.* **37**, 299–339 (2001).
13. E. J. Jumper and S. Gordeyev, "Physics and measurement of aero-optical effects: past and present," *Annu. Rev. Fluid Mech.* **49**, 419–441 (2017).
14. S. Gordeyev et al., "Comparison of unsteady pressure fields on turrets with different surface features using pressure-sensitive paint," *Exp. Fluids* **55**, 1661 (2014).
15. J. P. Siegenthaler, "Guidelines for adaptive-optic correction based on aperture filtration," PhD Thesis, University of Notre Dame (2008).

16. R. M. Rennie, D. A. Duffin, and E. J. Jumper, "Characterization and aero-optic correction of a forced two-dimensional weakly compressible shear layer," *AIAA J.* **46**, 2787–2795 (2008).
17. M. R. Kemnetz and S. Gordeyev, "Analysis of aero-optical jitter in convective turbulent flows using stitching method," *AIAA J.* **60**, 14–30 (2022).
18. J. Wells et al., "Experimental and computational investigation of laser beam propagation through a free shear layer," *Proc. SPIE* **12693**, 1269315 (2023).
19. W. Yanta et al., "Near-and farfield measurements of aero-optical effects due to propagation through hypersonic flows," in *31st AIAA Plasmadyn. and Lasers Conf.* (2000).
20. D. Neal, J. Copland, and D. Neal, "Shack–Hartmann wavefront sensor precision and accuracy," *Proc. SPIE* **4779**, 148–160 (2002).
21. J. Yu et al., "The suppression of aero-optical aberration of conformal dome by wavefront coding," *Opt. Commun.* **490**, 126876 (2021).
22. S. Gordeyev and M. Kalensky, "Effects of engine acoustic waves on aerooptical environment in subsonic flight," *AIAA J.* **58**, 5306–5317 (2020).
23. Y. Diskin et al., "Aircraft to ground profiling: turbulence measurements and optical system performance modeling," *AIAA J.* **59**, 4610–4625 (2021).
24. M. Kalensky et al., "Estimation of atmospheric optical turbulence strength in realistic airborne environments," *Appl. Opt.* **61**, 6268 (2022).
25. E. J. Jumper et al., "The airborne aero-optics laboratory, AAOL," *Proc. SPIE* **8395**, 839507 (2012).
26. M. Kalensky, S. Gordeyev, and E. J. Jumper, "In-flight studies of aero-optical distortions around AAOL-BC," in *Aviation Forum*, American Institute of Aeronautics and Astronautics (2019).
27. N. De Lucca, S. Gordeyev, and E. Jumper, "The airborne aero-optics laboratory, recent data," *Proc. SPIE* **8395**, 839508 (2012).
28. J. Morrida et al., "Shock-related effects on aero-optical environment for hemisphere-on-cylinder turrets at transonic speeds," *Appl. Opt.* **56**, 4814 (2017).
29. J. J. Morrida et al., "Simultaneous pressure and optical measurements around a hemispherical in subsonic and transonic flight," in *Aviation Forum*, American Institute of Aeronautics and Astronautics (2017).
30. M. Kalensky, J. Wells, and S. Gordeyev, "Image degradation due to different in-flight aero-optical environments," *Opt. Eng.* **59**, 104104 (2020).
31. R. Rennie et al., "Numerical investigation of a two-dimensional compressible shear layer and comparison to weakly compressible model," in *DEPS Beam Control Conf.* (2008).
32. M. Wang, A. Mani, and S. Gordeyev, "Physics and computation of aero-optics," *Annu. Rev. Fluid Mech.* **44**, 299–321 (2012).
33. M. Kalensky, "Airborne measurement of atmospheric-induced beam jitter," PhD Thesis, University of Notre Dame (2022).
34. M. Kalensky, "Branch-point identification using second-moment Shack–Hartmann wavefront sensor statistics," *Appl. Opt.* **62**, G101–G111 (2023).
35. J. Wells, R. Rennie, and E. Jumper, "An investigation into the thermodynamics of a weakly-compressible shear layer," in *AIAA Aviation 2020 Forum* (2020).
36. J. Wells, *Thermodynamic Behavior of a Weakly Compressible Shear Layer*, University of Notre Dame ProQuest Dissertations Publishing (2021).
37. E. Fitzgerald and E. Jumper, "The optical distortion mechanism in a nearly incompressible free shear layer," *J. Fluid Mech.* **512**, 153–189 (2004).
38. M. Kalensky, M. R. Kemnetz, and M. F. Spencer, "Effects of shock waves on Shack–Hartmann wavefront sensor data," *AIAA J.* **61**, 2356–2368 (2023).
39. J. H. Gladstone and T. Dale, "Researches on the refraction, dispersion, and sensitiveness of liquids," *R. Soc.* **153**, 317–343 (1863).
40. M. Kalensky et al., "In-flight measurement of atmospheric-imposed tilt: experimental results and analysis," *Appl. Opt.* **61**, 4874 (2022).
41. M. Kalensky, M. R. Kemnetz, and M. F. Spencer, "Effects of shock-related discontinuities on SHWFS measurements: modeling and simulation," *Proc. SPIE* **12239**, 122390J (2022).
42. M. Kalensky et al., "Branch-point detection using a Shack–Hartmann wavefront sensor," *Proc. SPIE* **12693**, 126930C (2023).
43. M. Kalensky et al., "Comparison of branch-point detection approaches using a Shack–Hartmann wavefront sensor," *Opt. Eng.* **62**, 123101 (2023).
44. A. E. Siegman, "How to (maybe) measure laser beam quality," in *DPSS (Diode Pumped Solid State) Lasers: Appl. and Issues*, OSA (1998).
45. D. L. Fried and J. L. Vaughn, "Branch cuts in the phase function," *Appl. Opt.* **31**, 2865 (1992).
46. F. de Souza, "Hot-wire response in compressible subsonic flow," *AIAA J.* **58**(8), 3332–3338 (2020).
47. R. Rennie, D. Duffin, and E. Jumper, "Characterization and aero-optic correction of a forced two-dimensional weakly compressible shear layer," *AIAA J.* **46**(11), 2787–2795 (2008).

48. R. Rennie, J. Siegenthaler, and E. Jumper, "Forcing of a two-dimensional weakly compressible subsonic free shear layer," in *AIAA Aerosp. Sci. Meeting and Exhibit* (2006).
49. G. Elliot and M. Samimy, "Compressibility effects in free shear layers," *Phys. Fluids A* **2**(7), 1231–1240 (1990).
50. M. Visbal, "Numerical simulation of aero-optical aberration through weakly-compressible shear layers," in *39th AIAA Fluid Dyn. Conf., 2009-4298* (2009).
51. H. Schlichting and K. Gersten, *Boundary-Layer Theory*, 9th ed., Springer Berlin, Heidelberg (2017).
52. W. Southwell, "Wave-front estimation from wave-front slope measurements," *J. Opt. Soc. Am.* **70**(8), 998–1006 (1980).
53. M. Kemnetz, "Analysis of the aero-optical component of the jitter using the stitching method," PhD Thesis, University of Notre Dame (2019).

Jonathan Wells is a research scientist at the Naval Information Warfare Center Atlantic. He received his BS degree in physics and astronomy from Indiana University South Bend, and his MS and PhD degrees in aerospace and mechanical engineering from the University of Notre Dame. His research interests include directed energy, optical communications, atmospheric propagation of lasers, and aero-optics.

Matthew Kalensky is an engineer at the Naval Surface Warfare Center Dahlgren Division. He received his BS degree in mechanical and materials engineering from Loyola University Maryland in 2017 and received his MS and PhD degrees in aerospace engineering from the University of Notre Dame in 2020 and 2022, respectively. He actively runs a cross-service adaptive-optics working group, is a chair for the Unconventional Imaging, Sensing, and Adaptive Optics conference at SPIE Optics and Photonics, and is the Webinar Officer for Optica's Laser System's Technical Group. His expertise and research interests are in beam control, deep-turbulence characterization, and aero effects.

R. Mark Rennie is a research professor in aerospace and mechanical engineering at the University of Notre Dame. He has been active in aero-optics research for more than 15 years, including fundamental research into the aero-optics and adaptive-optic correction of compressible shear layer flows.

Eric J. Jumper is the Roth-Gibson Professor of aerospace and mechanical engineering at the University of Notre Dame. He has worked in the areas of airborne lasers since his time as an Air Force officer in the 1970s. He retired from the Air Force as a lieutenant colonel and a director of the Laser Devices Division of the Air Force Research Lab in 1989. He has authored numerous papers in the areas of aero-optics, airborne lasers, and beam control, and he recently published a Wiley Science series book on aero-optics.